ELSEVIER

Contents lists available at ScienceDirect

# International Journal of Rock Mechanics and Mining Sciences

journal homepage: www.elsevier.com/locate/ijrmms



# Micromechanics of stick-slip deformation across rough faults

Eliaz Ishay<sup>a</sup>, Doron Morad<sup>a,b</sup>, Yossef H. Hatzor<sup>a,\*</sup>

- <sup>a</sup> Dept. of Earth and Environmental Sciences, Ben-Gurion University of the Negev, Beer Sheva, Israel
- <sup>b</sup> Present address: Dept. of Earth and Planetary Sciences, University of California Sanata Cruz, Santa Cruz, CA., USA

#### ARTICLE INFO

Keywords: Direct-shear Stick-slip Roughness Shear stiffness Critical stiffness Dilation Stress drop

#### ABSTRACT

We investigate how the initial surface roughness of laboratory faults, generated in stiff diabase rocks, affects the micromechanics of stick-slip oscillations with normal stresses ranging from 2.5 to 15 MPa. The tested surfaces spanned a wide range of roughness: from extremely smooth (Polished; RMS  $_{x=4mm}=0.83-1.33 \mu m$ ), to intermediate (Saw-cut; RMS  $_{x=4mm}=3.9-9.98 \mu m$ ), to extremely rough (Fractured; RMS  $_{x=4mm}=154-222 \mu m$ ). We show that both global shear behavior as well as dilation are strongly influenced by surface roughness and normal stress. By detrending the global dilation signal, we identify a clear relationship between vertical motion, roughness, and normal stress: the amplitude of vertical displacement during stick phases increases with normal stress and is maximized at intermediate (saw-cut) roughness levels. We confirm the 'critical roughness' concept previously identified by Morad et al., 2022, that predicts that the intermediate roughness (saw-cut) produces the largest stress drop magnitudes, across a wide range of normal stresses. Both smoother and rougher interfaces exhibit a more stable sliding behavior. Furthermore, a positive correlation between interface shear stiffness during stick-slip cycles  $(k_i)$ , normal stress  $(\sigma_n)$ , and sliding instability as scaled by mean stress drop  $(\Delta \tau)$  is firmly established, particularly for rougher interfaces. Finally, we introduce a new energy-based criterion to predict sliding instability potential. This novel approach links the stress drop magnitude during stick-slip cycles to both the intra-cyclic shear stiffness of the interface and the applied normal stress, all measurable quantities, and does not require the critical stiffness (kc) which cannot be measured directly, as used in rate and state friction laws.

### 1. Introduction

Catastrophic frictional failures such as earthquakes and landslides usually occur along pre-existing planes of weakness. The area of discrete contact and the strength of those contacts determine the shear strength of preexisting interfaces. <sup>1–3</sup> Therefore, variations in surface topography are among the key factors influencing their frictional behavior. 4-6 Surface roughness has been reported to influence also the stress distribution along fault zones<sup>7,8</sup> and fault nucleation and propagation as inferred from lab experiments and numerical simulations 9-12 and also based on earthquake observations. 13 Outcrops of faults have been found to present great variations in roughness, from extremely smooth<sup>14</sup> to very rough with aspect ratio of 0.0001–0.01 respectively. 15 Moreover, surface geometry is strongly coupled with dilation and increased joint aperture during shear, <sup>16,17</sup> enhancing fracture transmissivity and rock mass permeability, <sup>18,19</sup> which have practical implications in reservoir enhancement, wastewater injection, and CO<sub>2</sub> sequestration, <sup>20,21</sup> If flow is restricted, dilation of rough interfaces may affect the critical pore pressure required for slip, and at times may even impede slip. <sup>22–25</sup> In a seismological context, in particular for shallow earthquakes, slip across geological faults is often characterized by episodes of a quasistatic phase followed by dynamic unstable sliding commonly referred to as stick-slips. The frictional resistance during the quasi-static stage gradually increases while during the dynamic stage it drops abruptly to a lower value. <sup>26,27</sup> Recent studies show evidence for unstable motion also in a much shallower context than crustal geological faults, for example deep-seated landslides, <sup>28,29</sup> glacier sliding, <sup>30–32</sup> rock avalanches and granular flow, <sup>33</sup> induced seismicity, <sup>34,35</sup> and fault-slip rock bursts in tunnels and deep underground mining. <sup>35–37</sup> Hence, understanding the micromechanics, i.e. both normal and shear response of the rough interface during stick slip motion is essential for our understanding of fundamental rock friction, and for geohazard mitigation. <sup>38</sup>

The mechanism underlying stick-slip motion has been extensively studied, both experimentally and theoretically.  $^{39-41}$  In this simplified model, typically referred to as the "spring and a slider" analogue, a necessary condition for unstable sliding is that the stiffness of the slider k

E-mail address: hatzor@bgu.ac.il (Y.H. Hatzor).

<sup>\*</sup> Corresponding author

- defined by the slider frictional properties and the normal stress - is greater than the spring stiffness  $k_m$ , represents either the machine stiffness in the lab, or the elastic properties of the rock medium surrounding a fault in the field. Thus, due to the stiffness differences, when the system is loaded, the slider contracts less than the spring allowing the slider to accumulate elastic energy that is spontaneously released when the frictional load exceeds the frictional resistance of the slider, inducing spontaneous acceleration of the block.  $^{48}$ 

It has been shown that surface properties might influence the relationship between the machine and interface stiffnesses,  $^{10,49-51}$  including mineralogy, porosity, and surface roughness. In addition factors involving the loading conditions such as normal stress, temperature, and slip rate  $^{45,47,52,53}$  have also been found to play a significant role in determining the critical stiffness. All in all, most studies used planar saw-cut surfaces for determining the unstable nature of frictional sliding across rock discontinuities, but obviously those surfaces do not correctly represent the surface topography of faults, which typically exhibits roughness at a wide range of scales.  $^{54-56}$  Moreover, when shearing rough faults a post-peak steady state phase is not always reached, and extremely noisy stick slip oscillations constrain the ability to measure the required empirical rate and state parameters  $^{44,45,52}$  for calculating the critical stiffness  $\mathbf{k}_c$ .

A recent study by Morad et al.<sup>57</sup> introduced the 'critical roughness' concept, in which the stability of an experimental fault is roughness dependent with a specific roughness amplitude that prompts the highest stress drop magnitude. They found that very rough tension-induced or very smooth polished surfaces exhibited relatively stable sliding. It was also shown that for saw-cut roughness the vertical motions during unstable sliding advance "in phase" with the dynamic stress drops with clear dilation and contraction during the reloading (stick phase) and unloading (slip phase), respectively.

Nonetheless, the full understanding of the micromechanics of dilation in relation to surface roughness, especially during unstable oscillatory sliding (i.e. stick-slips) is still not well understood. To probe deeper into the micromechanics of stick slip deformation we performed multiple direct-shear experiments on Diabase laboratory faults in an attempt to clarify three main issues.

- 1. Can we observe any roughness dependent pattern in the micromechanics of stick slip deformation during sliding across rough faults, with emphasis on vertical motions?
- 2. Can we confirm the validity of the proposed "critical roughness" concept which was defined by Morad et al.<sup>57</sup> only for constant normal stress level of 5 MPa, for a broader range of normal stresses active at shallow depths?
- 3. Is it possible to formulate an energy-based criterion for the potential stress drop during the slip phase using the energy absorbed during loading (stick) segments of stick-slip cycles?

# 2. Materials and methods

All direct shear tests were conducted on Diabase samples from Shanxi Quarry in China, commercially known as "Black Granite". The Diabase is medium-grained (mean grain size of 0.4 mm) composed of 40 % Plagioclase, 40 % Clinopyroxene, 10 % Amphibole and 10 % oxides and other minerals. We use the same stiff Diabase samples for all tests to eliminate the contribution of variables such as mineralogy, porosity, density, and focus on the relationships between initial surface roughness and sliding instability under different normal stress levels. The choice of a relatively stiff starting material stems from our attempt to observe stick slip deformation in the lab during post-peak sliding. Such instabilities might be restrained given a softer starting material, as one of the conditions for sliding instability is that the stiffness of the interface is greater than the stiffness of the machine. <sup>45,46,52</sup> Indeed, the density of the rock is as high as 3.05 gr/cm<sup>3</sup> and the porosity as low as 0.73. Young's modulus

and Poisson's ratio of the intact material are 97 GPa and 0.19  $\pm$  0.02, respectively.

## 2.1. Roughness analysis

In this study, we examined a wide spectrum of surface roughness, which was categorized into three distinct levels of roughness amplitude from very smooth and polished surfaces to multiscale, rough, tension-induced fractures (see Table 1). The rationale for choosing these three roughness levels is twofold: 1) these artificial roughness profiles can easily be reproduced by any other rock mechanics laboratory in order to confirm the validity of our results, and 2) the obtained aspect ratio between roughness height (H) and sampling length (L) in our laboratory faults is between H/L = 1.07 %–0.006 % (see last column of Table 1), generally within the aspect ratio range characteristic of geological faults, typically between  $\sim 1$  % and  $\sim 0.1$  % (see Fig. 1 in Brodsky et al.,  $2016)^{58}$ ; it should be pointed out that extremely smooth fault planes that are not included in Brodsky et al. data set exhibit an H/L ratio as low as 0.001 %.  $^{14}$ 

The rough tension-induced faults were created by subjecting intact rock beams to four - point bending configuration, resulting in a natural tensile fracture propagating upward from an artificial notch created at the bottom of the beam, splitting it in half and creating two matching surfaces with multi-scale roughness geometry (RMS $_{\rm X}=_{\rm 4mm}$  of 154–222  $\mu m$ ). Saw-cut roughness was produced using an industrial rock-saw with average RMS $_{\rm X}=_{\rm 4mm}$  of 3.9–9.98  $\mu m$ . To create very smooth polished roughness, saw-cut surfaces were subsequently polished using fine carborundum grit powder generating characteristic RMS $_{\rm X}=_{\rm 4mm}$  of 0.83–1.33  $\mu m$ .

Surface roughness was carefully measured using two 3D optic laser profilometers. The so-called planar surfaces, namely saw-cut and polished, were scanned with the Nanovea ST-500 optic profilometer located at the BGU Earthquakes Physics Laboratory directed by Y. Tal, which employs an optical pen with maximum range, peak to valley, of  $\sim\!300~\mu m$  to measure distance. Rough tensile fractures were scanned at A. Sagy's lab at the Geological Survey of Israel, via Optimet's Connoscan-10 profilometer, using a lens with typical resolution of  $\sim\!1$ –5  $\mu m$ . To create a 3D mesh of the surface topography of the surfaces, multiple 2D profiles were scanned and brought together, and the unscanned area between profiles was computed by linear interpolation. For most samples we used sampling acquisition of 10  $\mu m$  along the shear direction and

**Table 1** Roughness RMS of all tested samples at two scales: x=4 mm for comparison the micromechanics features of all direct shear tests, and x=100 mm for estimating the laboratory fault aspect ratio H/L (%) to compare with real geological faults, where [H] is the extrapolated RMS for a sampling length [L] of 100 mm. Test Sawcut 15B\* utilized the same interface as test Sawcut 10C. All other interfaces were scanned for roughness analysis before any shearing took place.

Surface	σ <sub>n</sub> (MPa)	RMS x = 4 mm (\(\mu\) m)	RMS x = 100 mm ( <i>mm</i> )	Sample length (mm)	H/L (%)
Fractured	2.5	162	0.8807	102.00	0.88
Fractured	5	161	0.5375	108.2	0.54
Fractured	7.5	154	0.6599	105.94	0.66
Fractured	10	202	0.7066	95.67	0.71
Fractured	15A	222	0.5156	98.48	0.52
Fractured	15B	165	1.0714	101.04	1.07
Sawcut	2.5	8.7	0.0616	106.70	0.06
Sawcut	5	8.61	0.0402	102.65	0.04
Sawcut	10A	8.48	0.0572	102.35	0.06
Sawcut	10B	3.9	0.0626	101.28	0.06
Sawcut	10C	9.98	0.0274	98.83	0.03
Sawcut	15A	9.3	0.0612	102.03	0.06
Sawcut	15B*	9.98	0.0274	98.83	0.03
Polished	2.5	0.96	0.0076	107.50	0.008
Polished	5	0.83	0.0060	103.00	0.006
Polished	10	1.26	0.0086	103.67	0.009
Polished	15	1.33	0.0117	104.44	0.012

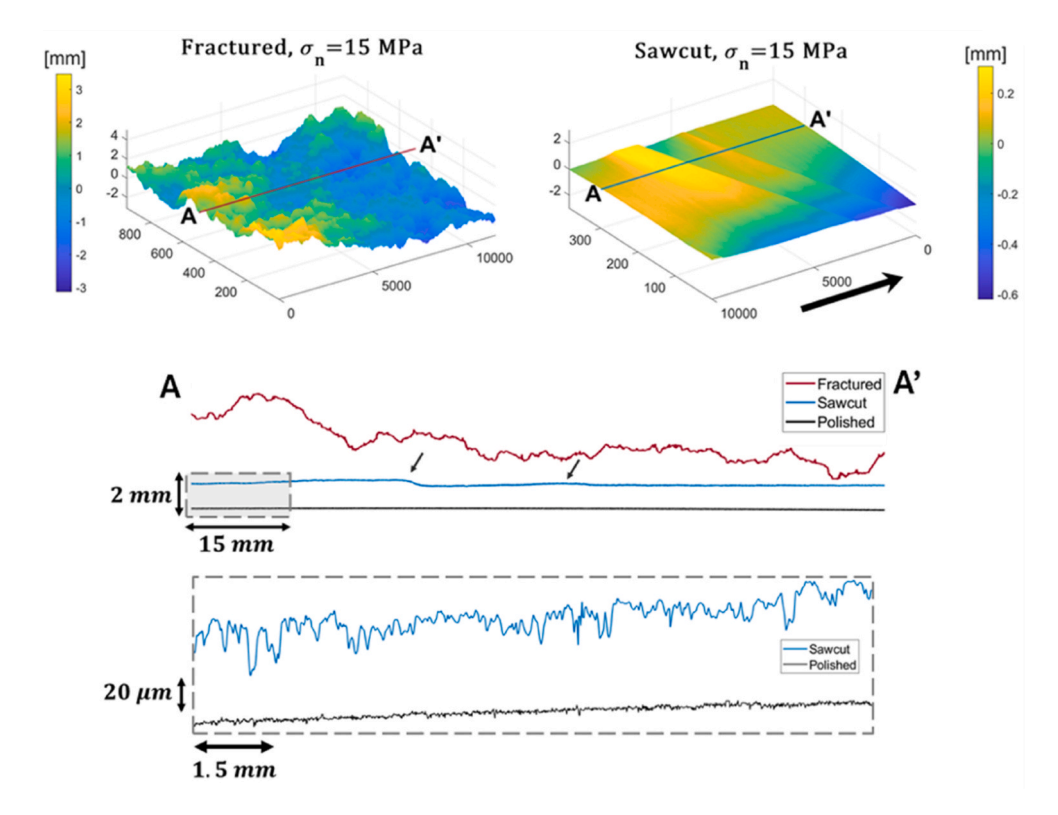


Fig. 1. Digital imaging of selected Fractured and Saw-cut surfaces, presented as 3D surfaces (top) and 2D representative profiles (bottom) corresponding to the A-A' lines marked on the surfaces. The black arrow indicates the sliding direction. Small black arrows in the lower panel point to large topographic relief of the Saw-cut sample compared to the Polished.

50  $\mu m$  perpendicular. This means that for a standard sample with a scanned surface area of 100  $cm^2$ , the scan output comprises at least  $2^*$   $10^7$  data points (Fig. 1).

Quantifying the roughness measurements was done by statistically calculating the root mean squares (RMS) of elevations from a mean reference for each profile along the intended shear direction, and then averaging the values of all profiles:

$$V(RMS) = \sqrt{\frac{1}{L} \int_{0}^{L} Z^{2}(x) dx}$$
 (1)

where L is the profile length, z is the height and x is the distance along the profile. The RMS value is a scale dependent function,  $^{59}$  which provides the roughness amplitude of a surface for any given length. For a better comparison between surfaces, we chose a length-scale of 4 mm (see 3rd column in Table 1), in correspondence with Morad et al.  $(2022)^{57}$  because at this level of roughness we can capture the logarithmic power law relationship between roughness in RMS and length.

The results of the statistical roughness analysis are presented in Fig. 2, revealing clear clustering among the roughness levels of the fractured, saw-cut, and polished surfaces.

# 2.2. Experimental

Direct shear tests were executed using the TerraTek hydraulic closed-loop servo-controlled direct shear system, at BGU Rock Mechanics Laboratory, in accordance with the ISRM suggested method. Rough fractures were assembled and cast in a perfectly mating configuration, resembling an interlocked fault or rock joint. The direct shear system comprised shear and normal pistons, with loading capacities of 300 kN and 1000 kN, respectively. The study involved three roughness levels (i. e., Polished, Saw-cut and Fractured), each was sheared under four different constant normal stress levels (2.5, 5, 10 and 15 MPa). One

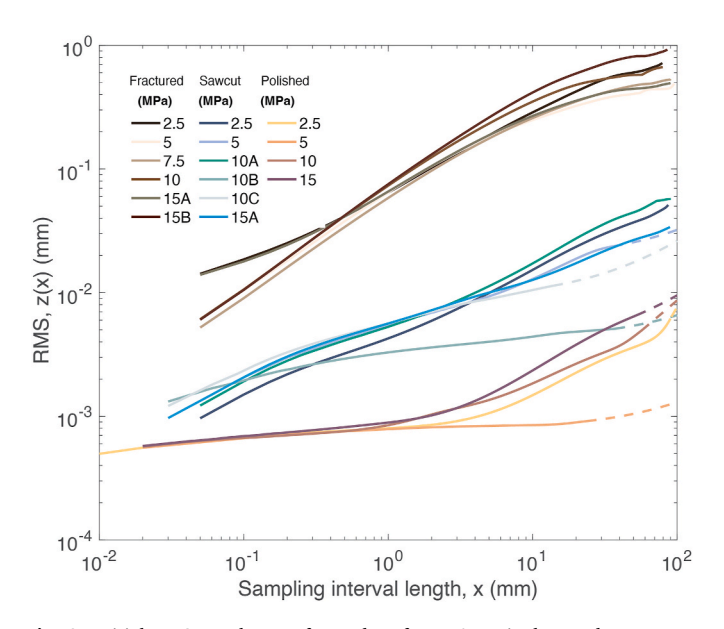


**Fig. 2.** Initial RMS roughness of tested surfaces. Any single trend represents RMS calculations of hundreds of profile lengths where z and x are the height and distance along the profile, respectively (see Equation (1)). Three surface types are shown: Fractured, Sawcut, and Polished. The three columns in the inset provide a color code for the normal stresses applied in each of the direct shear tests that were caried out on these surfaces. Capital letters A, B, C indicate tests performed under the same level of normal stress (e.g., 10A, 10B, 10C) but each time on a virgin surface. Dashed lines represent interpolated sections. (For interpretation of the references to color in this figure legend, the reader is referred to the Web version of this article.)

intermediate normal stress level of 7.5 MPa was applied on a rough tension-induced fracture.

Some tests were repeated due to technical issues. For example, direct shear tests conducted under the high end of normal stresses tested here, 15 MPa, sometimes were interrupted as the shear piston could not deliver the required force when operating under Low hydraulic power supply mode (note that assuming a sample area of 0.01 m<sup>2</sup> and a shear stress capacity of 300 kN, conducting a test under 15 MPa normal stress with a peak friction coefficient of 1 would require about 50 % of the shear piston capacity). In such instances we had to switch to High hydraulic power supply mode in the middle of the test which affected the output. In such cases the tests were repeated, under High hydraulic power supply mode, from the beginning. Our criterion for test repetition (each time using a new virgin surface) was: retesting until at least one complete, uninterrupted, test run was obtained for each roughness-normal stress combination. We note that in one case (Sawcut 10C) the same interface was sheared again under normal stress of 15 MPa (Sawcut 15B - not shown in Fig. 2) because extremely small damage area was detected at the termination of test Sawcut 10C. All tests, including those affected by minor technical issues, were retained in the dataset, as the obtained deviations were relatively small, but the results remained scientifically valuable, resulting in a total of 17 direct shear tests conducted in the framework of this study, as detailed in Table 2.

The test procedure began with the application of normal stress at a constant loading rate of 0.01 MPa/s until the target normal stress was reached. A good indication of a perfectly mating assembly is a quiet normal loading segment with no audible acoustic emissions, indicating that no significant horizontal rearrangement of the surfaces was required to accommodate the normal loading. All shear tests were performed under constant shear displacement rate of 0.01 mm/s and under piston displacement control (PDC). This setup allows the interfaces to experience sliding instabilities freely without intervention of the servo control system due to displacement output coming from the LVDTs that are mounted close to the interface (see below), better reflecting stick-slip sliding instabilities and field boundary conditions on slip of geological faults. 61 During shearing, the upper box was free to move vertically, as the tests were performed under imposed constant normal load boundary condition (CNL). Displacement between the surfaces was precisely monitored using 2 horizontal LVDTs mounted near the shear interface and 4 vertical LVDTs mounted on each corner of the upper shear box (Fig. 3a), enabling careful examination of the dilatational behavior of the laboratory faults during shear. Typical sliding distance was set to 10–12 mm, depending on sample size, and data acquisition rate was set to 50 Hz in all tests.

#### 3. Data

We perform 17 direct shear tests in this study. For each test we measure the surface topography using a laser profilometer. Once the target normal stress is obtained, shear stress is applied until reaching a maximum value followed by the residual stage where stable or unstable sliding is observed. While sliding at residual strength conditions each stick slip cycle is characterized by a loading phase (stick) followed by an abrupt and spontaneous unloading phase (slip). For our micromechanics analysis we used only the residual friction stage of the test although stick slip deformation may sporadically be encountered during the initial loading stage to maximum shear strength. For all analyzed stick slip oscillations we measure the initial shear stiffness  $k_i$ , defined as the elastic reloading slope of the interface within stick-slip cycles, and the stress drop magnitude  $\Delta \tau$ . Shear stiffness  $k_i$  scales the ability of two contacting surfaces to resist shear deformation and is governed by the degree of initial interlocking between asperity population and the elasticity of the bulk material. We measure the shear stiffness using the slope of the linear elastic segment of each reloading curve, from  $\tau_{min}$  to 50 %  $\tau_{max}$ , calculated via least-squares linear regression fit and divided by the corresponding creep displacement taking place during stick phases (see Fig. 4):

$$k_i = \left(\frac{\Delta \tau}{\Delta u}\right)_{reloading} \tag{2}$$

The unloading slope (Fig. 4, blue line) represents the machine stiffness  $k_{\infty}^{26}$ :

$$k_m = \left(\frac{\Delta \tau}{\Delta u}\right)_{unloading} \tag{3}$$

 $k_m$  can also be calculated by measuring the difference in shear displacement between the load piston and the shear box, which scales the evolution of shear stress over the amount of contraction in the system spring during each reloading segment due to system compliance<sup>61</sup>:

$$k_{m} = \left(\frac{\Delta \tau}{\Delta u_{(piston)} - \Delta u_{(shear-box)}}\right)_{reloading} \tag{4}$$

Global dilation of the faults is denoted as  $\Delta \nu$ , while microdilatational behavior during stick and slip phases is denoted as  $\Delta \nu_{stick}$  and  $\Delta \nu_{slip}$ , respectively (also shown in Fig. 4):

$$\Delta v_{stick} = v_{(peak_{(i+1)})} - v_{(min_{(i)})}$$
(5)

$$\Delta v_{slip} = v_{(peak_{(i+1)})} - v_{(min_{(i+1)})}$$

$$\tag{6}$$

Table 2 Concentrated results of all direct shear tests conducted in this study, arranged by surface finish type. For meaning of symbols see text.  $\Delta V$  is the ultimate dilation of the interface. Sample Sawcut 15B\* (not shown in Fig. 2) is a second run of sample Sawcut 10C. This is the only case where the same surface was sheared more than once.

Surface	$\sigma_n$ (MPa)	$\sigma_p$ (MPa)	$\sigma_r$ (MPa)	$k_s$ (MPa/mm)	$k_i$ (MPa/mm)	$\Delta \tau \; (MPa)$	$\Delta V\left(mm\right)$
Fractured	2.5	2.33	2.28	5.38	11.6	0.18	0.2579
Fractured	5	4.26	4.01	10.23	13.4	0.25	0.1385
Fractured	7.5	7.9	5.93	8.37	22.3	0.74	0.179
Fractured	10	10.64	7.85	21.37	15.4	0.46	0.0979
Fractured	15A	15.37	11.54	25.28	22.4	0.71	0.9348
Fractured	15B	15.96	8.97	20.32	27.3	1.33	1.286
Sawcut	2.5	1.92	1.84	15.4	17.8	0.27	-0.24
Sawcut	5	4.56	4.33	43	35.3	0.64	-0.001
Sawcut	10A	8.25	8.07	21.9	46.2	0.82	0.1704
Sawcut	10B	9.14	9.09	51.2	61.1	0.85	0.0391
Sawcut	10C	9.85	9.85	9.1	20.3	2.61	-0.04
Sawcut	15A	11.69	11.31	46	41.6	1.95	0.0759
Sawcut	15B*	12.57	12.55	19.5	25.5	4.13	0.0382
Polished	2.5	2.23	2.23	91.3	0	0	-0.037
Polished	5	3.37	3.37	17.4	16.9	0.04	-0.13
Polished	10	7.52	7.52	_	34.3	0.26	-0.011
Polished	15	12.13	11.63	23.5	30.4	0.35	-0.167

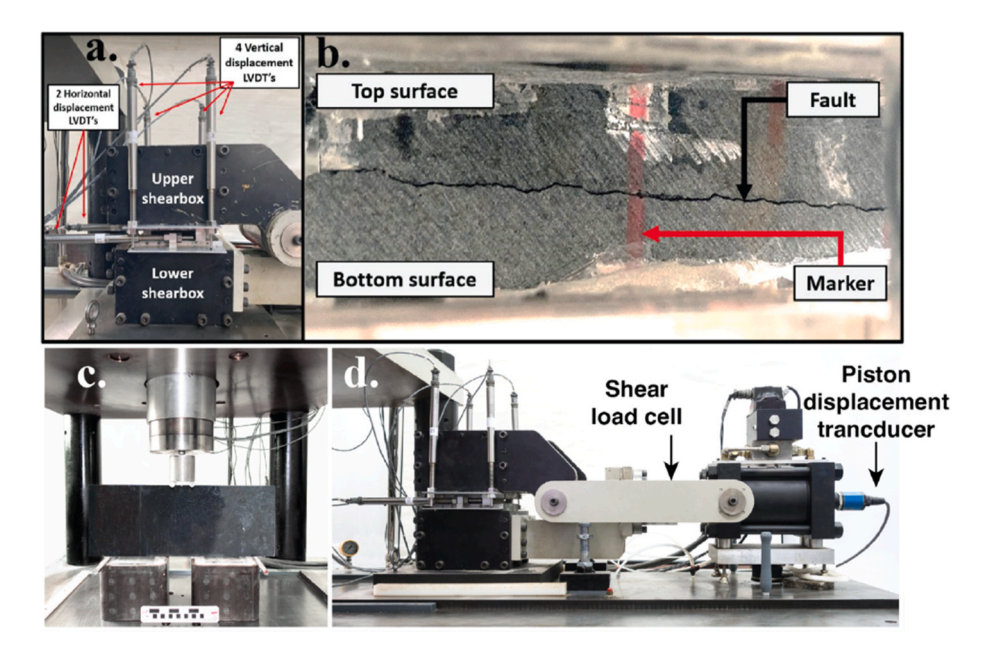
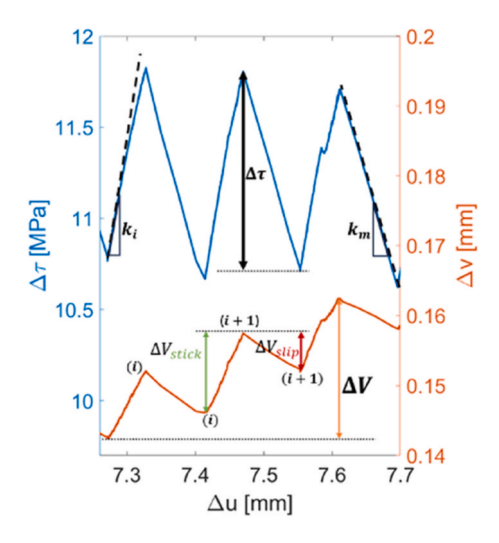


Fig. 3. The direct shear system and test assembly. a. The shear box, including the four vertical and two horizontal LVDT transducers, b. Perfectly mating initial configuration of rough surfaces before shear. Note the red marker indicating the correct alignment of the two blocks, and the clear rough non-planar fault separating them. c. The normal load frame, here showing a four-point bending test configuration, d. the shear load frame including the location of the shear load cell and the piston displacement transducer. (For interpretation of the references to color in this figure legend, the reader is referred to the Web version of this article.)



**Fig. 4.** Shear stress (blue) and normal displacement (orange) vs. shear displacement during oscillatory stick-slip cycles. The stiffness and stress drop parameters are presented on the shear stress curve, while the vertical motion parameters are presented below on the normal displacement curve. (For interpretation of the references to color in this figure legend, the reader is referred to the Web version of this article.)

## 4. Results

### 4.1. Macro frictional behavior

Concentrated results of all direct shear tests are tabulated in Table 2. The evolution of shear stress (upper panels) and vertical displacement (lower panels) with shear displacement are presented in Fig. 5. For each level of initial roughness, we conducted at least 4 different direct shear experiments under normal stresses varying between 2.5 and 15 MPa. We find that in planar (polished and saw-cut) surfaces shear stress gradually increases, eventually stabilizing at some residual level without exhibiting a distinct peak shear stress. Polished interfaces were characterized

by strain hardening after reaching a local peak, with notable stick-slips observed only when the sheared interface was subjected to a normal stress of 15 MPa and beyond 6 mm displacement. The saw-cut surfaces exhibited residual friction during which stick slip deformation prevailed. Rough fractured surfaces exhibited similar sliding behavior under low normal stresses of 2.5 and 5 MPa, while under higher normal stresses the shear stress – shear displacement curve segmented into two distinguishable phases of peak and residual sliding, where under 15 MPa normal stress the transition from peak to residual strength was followed by an audible and sizeable stress drops (Fig. 5). Saw-cut interfaces reached their peak friction including significant stick-slips after ~4 mm of sliding, while the initiation of stick slip motion in fractured surfaces ensued after 3-4 mm of sliding. Polished surfaces typically did not exhibit transition from peak to residual friction. The Polished and Sawcut surfaces consistently exhibited moderate compression throughout the entire test whereas rough interfaces (fractured) exhibited an initial compression phase followed by a significant dilation of the upper block as sliding progressed. Interestingly, the ultimate dilation of the surfaces did not exhibit a clear linear relationship with normal stress, probably manifesting two competing mechanisms of riding on asperities vs. truncation of asperities in "shear off" mechanism. 59

Rough surfaces showed visible wear around topographic irregularities with detectable damage primarily focused at the center of the sheared interfaces. Sawcut interfaces exhibited striations with smeared gray-white wear powder, where the area of the smeared layer is proportional to the normal stress. Polished surfaces showed barely any detectable damage under low normal stresses but only under 15 MPa, abrasive wear was observed (Fig. 6). Rough surfaces exhibited extensive wear and gouge formation across the interface, indicating intense brittle deformation during shear, under all normal stress levels.

## 4.2. Micro mechanical deformation

In this section, we examine the micro mechanical behaviour during stick slip oscillations in terms of the intracycle stress drop, the consequent vertical displacement and the shear stiffness. For each experiment, we defined the residual frictional value (usually after 3–4 mm of displacement) and neglected events before that. We used a shear stress

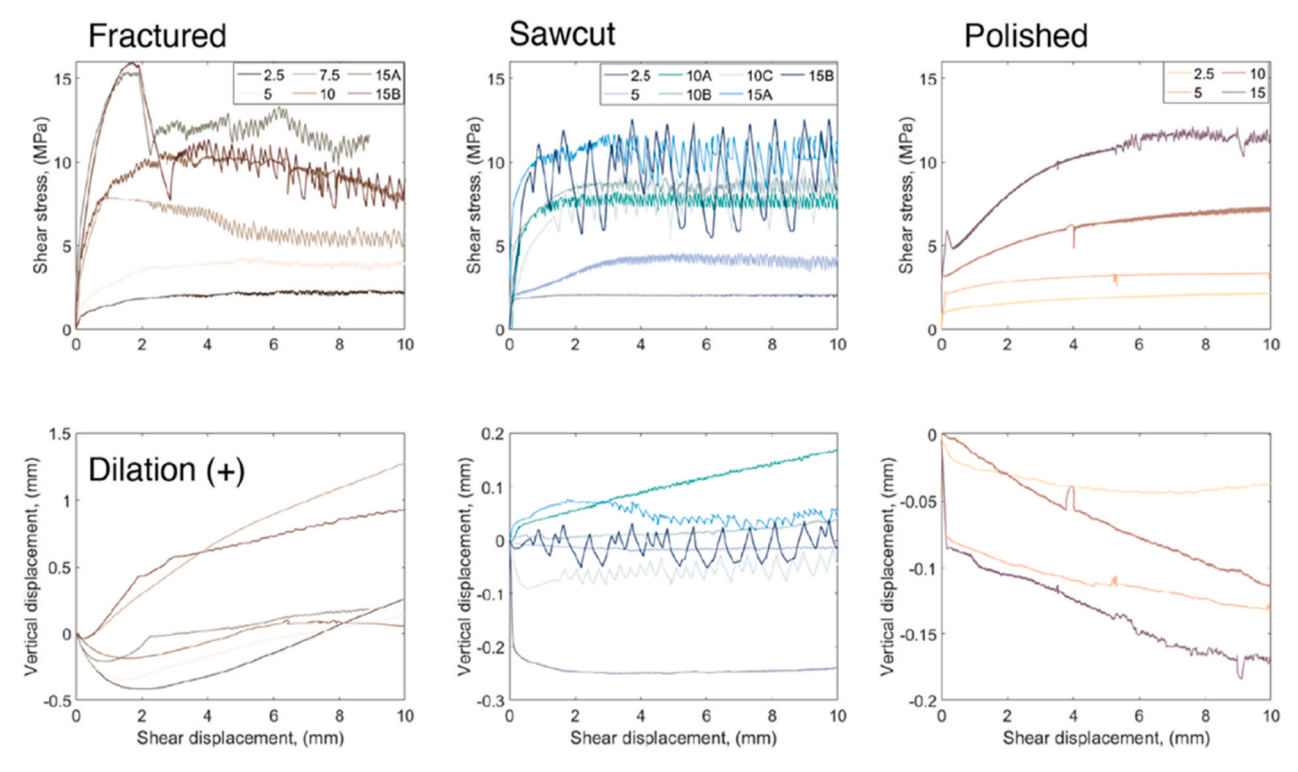


Fig. 5. Shear stress (upper panels) and Vertical displacement (lower panels) vs. shear displacement for Fractured (left) Sawcut (center) and Polished (right) surfaces. Note here dilation is positive.

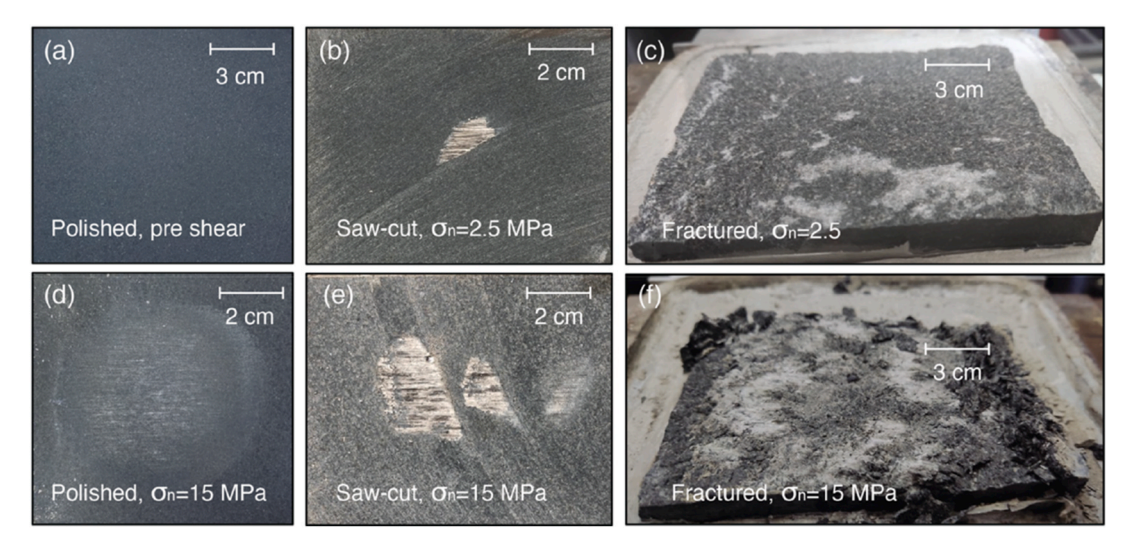


Fig. 6. Representative polished interface before (a) and after (d) shear under 15 MPa Normal stress; Post shear damage under 2.5 MPa and 15 MPa normal stress for sawcut (b, e) and fractured (c, f) surfaces.

threshold of 0.1 MPa for defining a stick slip event, a value 10 times higher than the shear load data acquisition noise, which is  $\sim$ 0.01 MPa.

# 4.3. Micro-dilatational behavior

Fig. 7 presents representative snapshots of shear stress and dilation during stick-slip cycles in our three data groups. We use those representative timelines specifically because the sample at that stage is presumably at steady state. We defined micro-dilatational behavior of the surfaces during stick-slip cycles as the force (blue) and vertical (red) outputs of the load cell and the four vertical LVDTs, respectively.

Sawcut surfaces usually exhibit "in phase" stick-slip oscillations and dilatational behavior of the surfaces. These surfaces consistently dilate

during stick segments and compress during slip segments, regardless of the normal stress applied, except for the sawcut surface sheared under 2.5 MPa normal stress. We attribute this anomaly to an imperfect alignment of the bottom and upper surfaces during sample assembly, as the planar surfaces are very difficult to perfectly level at a completely mating configuration. Overall, the in-phase dynamic behavior exhibited by the sawcut surfaces implies that the governing deformation mechanism acting upon sawcut interfaces during unstable shear motion is climbing over asperities rather than shearing through them.

Due to their significant roughness, Fractured surfaces strongly exhibit global interface dilation during shear (Fig. 5). To compensate for this global trend and make comparisons between roughness levels meaningful, we detrend the global vertical displacement data in order to

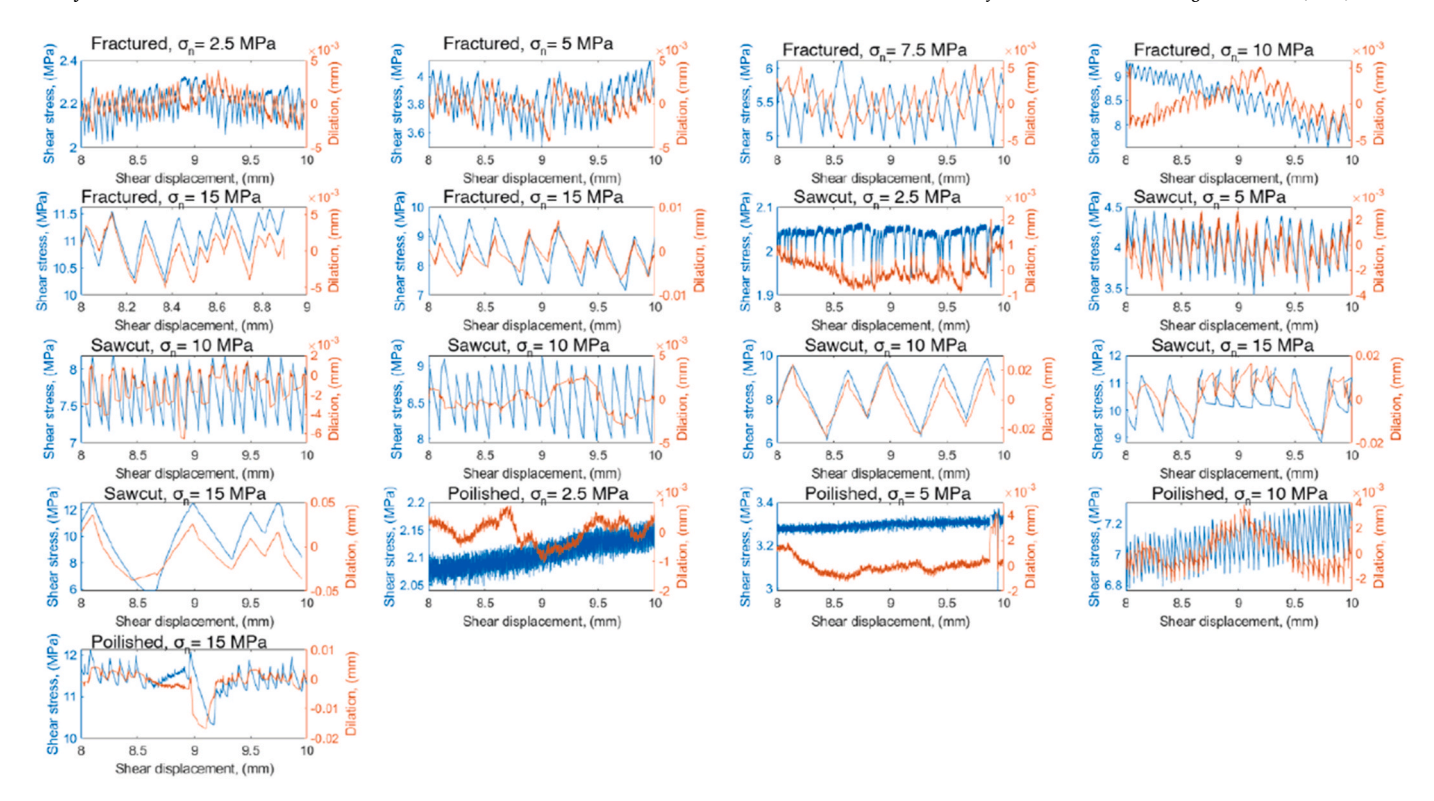


Fig. 7. Shear stress and normal displacement (dilation) vs. shear displacement: selected areas from the residual segment for selected experiments conducted on Fractured, sawcut, and polished interfaces.

isolate the vertical motion during stick slip episodes. Because the maximum dilatancy of Fractured interfaces is in the order of 1 mm (last column in Tale 2) and the sliding distance is greater than 10 mm (5th column in Table 1), the rotational effect can be neglected in detrending the data.

The detrended micro-dilatational behavior of the Fractured interfaces is more complex (see Fig. 7). Under low normal stress levels of 2.5, 5, and 7.5 MPa, opposite to the observations from the Sawcut interfaces, the Fractured interfaces compress during stick segments and dilate during slip segments. This behavior could be interpreted as damage concentrating at asperity tips in the rougher surfaces giving rise to brittle deformation during the stick phase, manifesting in interface compression during stick segments. Interestingly, however, under 10 and 15 MPa normal stress studied here, the dilatational behavior of the Fractured surfaces resembles that which is observed for the Sawcut interfaces, with distinct dilation during stick phases followed by compression during slip phases.

We suggest that the transition from contraction to dilatancy during the stick phase implies heterogeneous and intense stress concentrations at asperity tips during the normal loading segment up to 15 MPa as well as through the shearing segment, leading to increased damage at asperity tips. As shown in Fig. 6, this damage does not penetrate deeply into the interface but instead shears the tallest asperities, leading to a homogenization of the interface and a smoother statistical roughness thus altering the surface characteristics closer to those of a sawcut interface topography. Consequently, the obtained dilatational behavior of the initially Fractured surfaces during shear under this relatively high level of normal stress resembles that which is observed for sawcut interfaces.

In the case of the polished surfaces, no apparent coupling is observed between stick-slips and dilation, although under higher normal stresses, dilation appears to be constrained to the stick phases.

## 4.4. Micro-shear resistance

Fig. 8 presents intracyclic shear stiffness  $k_i$  and machine stiffness  $k_m$  (upper panels) and stress drop magnitude  $\Delta \tau$  (lower panels) as a function of the normal stress. The machine stiffness  $k_m$  remains constant within and in between tests with a mean value of  $\sim \! 10.63$  MPa/mm and therefore does not seem to be affected by surface conditions and normal stress level. The intracyclic shear stiffness is very sensitive to the roughness and normal stress levels. The sawcut surfaces generally exhibit the highest shear stiffness, as also found by Morad et al.. <sup>57</sup> In contrast to shear stiffness, the stress drop magnitude, as would be intuitively expected, increases with increasing normal stress, at all roughness levels studied.

The positive relation between  $\Delta \tau$ - $k_i$  peaks at a critical roughness amplitude, corresponding to the initial sawcut roughness, as under each level of normal stress applied the sawcut surfaces recorded the highest  $k_i$  values and correspondingly, the greatest laboratory earthquakes, as scaled by  $\Delta \tau$ .

#### 5. Criticality

## 5.1. Vertical motion criticality

Results of micro-dilatational behavior as a function of surface roughness are presented in Fig. 9. When calculating dilation, we only consider the reloading stage of each stick slip cycle because at that stage, the sample is maintaining force equilibrium and therefore the mechanical output is better constrained. Each data point in this figure represents the averaged vertical motion during the stick slip phase from 8 mm to 10 mm of global sliding distance. As mentioned above, we used this distance because it is as close as we can get to the residual stage in the global direct shear test output. We consider the governing mechanism for dilation at this stage as riding over asperities, while contraction might represent shearing off, or compression of asperities.

The experiments on polished interfaces exhibit stable sliding under

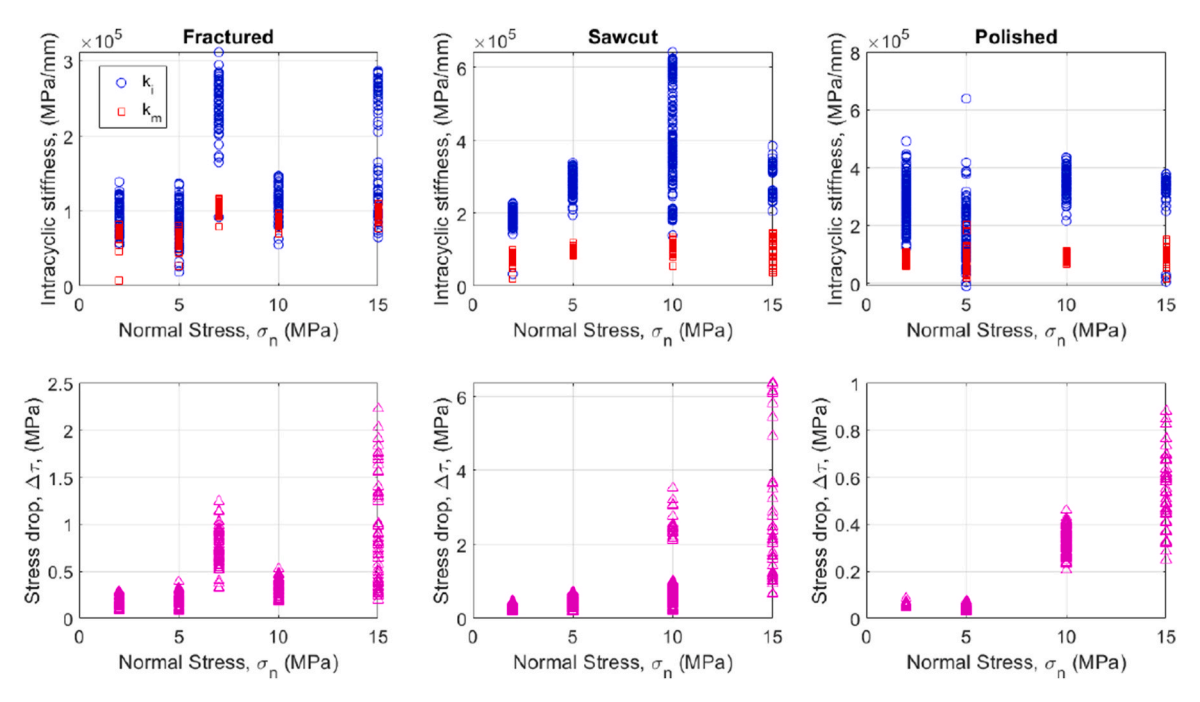
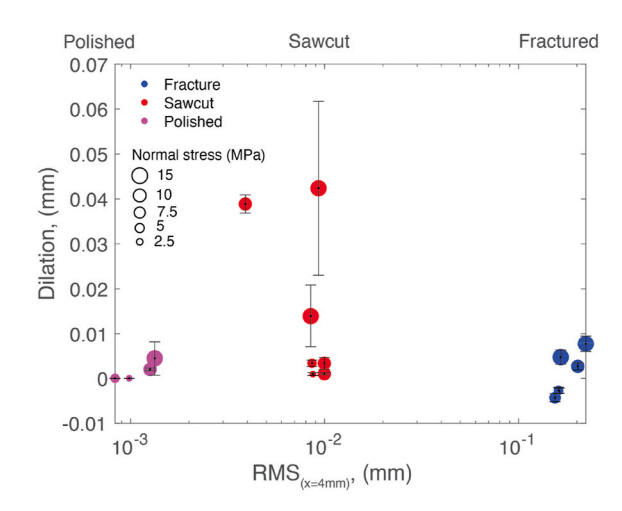


Fig. 8. Intracyclic shear  $(k_i)$  and machine  $(k_m)$  stiffness (upper panels) and stress drop magnitude (bottom panels) as a function of the normal stress for the three roughness groups.



**Fig. 9.** Average dilation of Fractured, Sawcut, and Polished surfaces during the reloading segments of stick slips. Measurements are made during "steady state" sliding, at global shear distance between 8 and 10 mm. The surface type is marked in solid circles that are scaled to the level of normal stress.

low normal stress and therefore there are no recorded vertical motions. Under higher normal stress, however, we observed very minor dilatancy during the stick phase, which moderately increased with increasing normal stress.

The sawcut interfaces present significant dilation (Fig. 9) with perfect coupling between dilation and shear stress oscillations (Fig. 7). Typically, we observe increased dilation with increasing normal stress, albeit with larger error bars (see Fig. 9). Interestingly, sawcut interfaces exhibit the highest values of dilation compared to the two endmembers of our studied roughness spectrum. It is also important to note that within stick slip motion, the magnitude of displacement during slip stages is typically in the order of  $\sim\!50~\mu m$  while the dominant roughness wavelength of the sawcut interfaces is in the order of  $\sim\!10~mm$ , therefore this is not a roughness-induced artifact.

The case of the fractured interfaces is more complicated, as already

mentioned in section 4.3 (see Fig. 7). Under low normal stresses of 2.5–7.5 MPa, we observed contraction during the reloading stage, possibly due to brittle fracture of asperity tips at this stage. In the case of the higher normal stresses of 10 and 15 MPa tested here, we propose that asperity tip damage, both during the normal loading segment as well as during the shear segment, leads to homogenized damage distribution across the sheared interface, so that when shearing commences, the dilatant response resembles that which is observed for sawcut surfaces, with stick and dilation in phase. But as indicated in Fig. 9, the absolute value of dilation in the fractured interfaces is much lower than that which is measured for the sawcut surfaces. This supports our assumption that during the normal loading segment fracture of asperities led to less pronounced peaks and valleys possibly leading to a more homogeneous surface topography with stick and dilation in phase during shear.

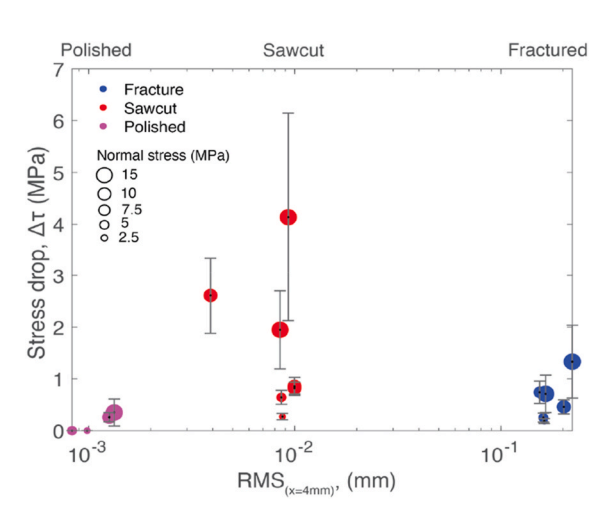


**Fig. 10.** Stress drop vs. initial roughness, measured at length scale of 4 mm for different levels of normal stress and surface roughness. Error bars on each marker represent the variance in all stress drops.

#### 5.2. Stress drop criticality

The relationship between surface roughness and stress drop is illustrated in Fig. 10. The results presented in Fig. 10 reflect data acquired from stick-slip cycles occurring along the residual strength segment, sometimes referred to as the "steady state" stage. The greatest stress drop we obtained in this study ( $\Delta \tau = \sim 8$  MPa) does not belong in this data set as it was recorded during the transition from peak to residual sliding of a fractured interface (Table 2) sheared under 15 MPa normal stress (first stress drop in upper left pane of Fig. 5). The significant peak strength we observed in this test ( $\mu = \sim 1.07$ ), suggests that while sawcut surfaces exhibit the highest shear stiffness  $k_i$  and stress drops  $\Delta \tau$ during stick-slip cycles, the level of interlocking of perfectly mated rough surfaces at the initiation of sliding is far greater. It can be seen that under each normal stress level applied, sliding instability peaks at a specific initial roughness, corresponding to the sawcut surfaces, and decreases towards the endmembers of our studied roughness spectrum: very smooth (polished) or very rough (fractured) surfaces. As would be expected, the stress drop magnitude does increase with increasing normal stress but non-linearly. For instance, the stress drop in the sawcut interfaces increases much more with increasing normal stress compared to the two endmembers.

## 6. Discussion

We begin the discussion with confirmation of the 'critical roughness concept' suggested by Morad et al.  $^{57}$  and then discuss in detail the micromechanics of stick slip deformation across planar and fractured laboratory faults, with emphasis on vertical (dilational/contractive) movements and the effect of normal stress.

## 6.1. Confirmation of the 'critical roughness' concept

In Fig. 10 we show that for each level of normal stress applied (2.5–15 MPa), the initial RMS roughness value of approximately 10  $\mu m$ , corresponding here to the sawcut interfaces, generated the highest magnitudes of stress drops and dilation during stick-slip cycles, an important finding that corroborates and expands the 'critical roughness' concept originally proposed by Morad et al. <sup>57</sup> who have limited their tests to a single normal stress level of 5 MPa due to the marginal stability conditions on this normal stress level.

In another recent study on laboratory Granite faults, Meng et al.,  $^{62}$  compared the sliding instability of rough tension-induced fractures to planar sawcut surfaces in direct shear tests under varying constant normal stresses of 1–50 MPa. They reported that while rough fractures constantly generated regular stick-slips with stress drop magnitudes increasing with normal stress, their planar surfaces, which are more similar to our polished surfaces in terms of mean roughness amplitude (with RMS roughness of  $\sim 2~\mu m$ ), produced stable sliding under all normal stresses, with significant dynamic stress drops and stick-slips occurring only under 50 MPa normal stress. As in Morad et al.,  $^{57}$  they also attributed the observed stable sliding of very smooth surfaces under relatively low normal stresses to the negligible mechanical interlocking and stress concentrations at asperity contacts while shearing across very smooth surfaces.

We find that like stress drop, shear stiffness is highest for the sawcut roughness across all normal stresses (Fig. 8), also consistent with Morad et al.  $^{57}$  observations. As has been well established, the magnitude of stress drop  $\Delta \tau$ , depends on the relationship between the loading system stiffness  $k_m$  and the critical stiffness of the surface  $k_c$ , the latter of which is influenced by surface roughness and normal stress, among other factors. However,  $k_c$  can not be directly measured in the lab and can only be derived from rate-and-state empirical fitting parameters  $(A, B, D_c)$  that can only be acquired accurately during true steady-state sliding because noisy stick-slip oscillations during the residual strength segment completely obscure the ideal steady state behavior presented for

example by Dieterich<sup>42</sup> or Ruina.<sup>45</sup> Indeed, their stable steady-state sliding was essential for determining their rate and state parameters, isolating the relationship between shear strength, stiffness, and other properties, but it may not fully represent natural conditions where roughness and complex surface interactions significantly influence mechanical behavior. In contrast, the shear stiffness  $k_i$  can be directly measured in the laboratory, regardless of surface roughness or unstable shear behavior. In addition, the triple relationship between  $k_i$ ,  $\Delta \tau$ , and  $\sigma_n$ is firmly established in this study, especially for rough interfaces. We therefore propose that the  $k_i$ - $k_m$  relationship may be a better proxy for sliding instability in real geological faults rather than the traditional  $k_c$ - $k_m$  model. 45,50 The data presented in Fig. 8 support this argument by showing that larger  $k_i$ - $k_m$  differences lead to higher stress drop magnitudes  $\Delta \tau$ , regardless of surface finish and in correlation with normal stress. We argue here that experimentally derived  $k_i$ - $k_m$  relationship provides a more reliable proxy for assessing fault stability as it can also be applied for rough surfaces and noisy sliding behavior.

Similarly to the critical stiffness as portrayed by Ruina  $^{45}$  ( $k_c = \sigma(A-B)/d_c$ ), we also observed an increase in shear stiffness with increasing normal stress, strengthening the statement that the intracycle shear stiffness can be a good proxy for the critical stiffness but with a very clear dependency on fault roughness.

## 6.2. Micromechanics of dilation

A novel aspect of the work reported here is the relationship between dilation and stick-slip motion, as a function of roughness and normal stress. Moreover, we discover that dilation also exhibits criticality, peaking during shear of saw-cut surfaces and declining towards the smooth and rough end members of the tested roughness spectrum.

We find that post-shear damage observed in planar surfaces includes striations, slickensides, and powder-size wear particles, which might be the result of decapitating interlocked asperity-tips when slip is initiated. Micro-scale examination of saw-cut surfaces during stick-slip cycles reveals a distinct dilation during stick phases and contraction during slip phases, with moderate correlation of the applied normal stress (Fig. 9). This dilation pattern, synchronized and in-phase with the stick-slip oscillations, resembles gliding over asperities, rather than shearing them off. Chen et al. 63 conducted rotary shear tests under constant normal stress and shear velocity (10.2–14.3 MPa and 0.26–617  $\mu m/s$ , respectively) on saw-cut surfaces, and suggested the same asperity interactions of riding on asperities.

Visual inspection of post-shear interfaces (Fig. 6) reveals that the Fractured surfaces exhibit larger damaged areas with increasing normal stress. The multiscale roughness of those interfaces is presumably more favorable to different asperity interaction mechanisms, such as shearing-through asperities, or even decapitating asperity tips, as normal stress is increased.

### 6.3. Implications to natural faults

We have shown that the concept of critical roughness remains valid to normal stresses up to 15 MPa, which is relevant to shallow engineering geology applications (e.g. volcanism, landslides, tunnels, dam foundations) and to deeper seismological processes (e.g. shallow earthquakes, induced seismicity, glacier motion) which are usually related to lower crustal depths. Our laboratory findings suggest that, beyond fault zone material, surface roughness plays a critical role in the emergence of these instabilities for a broad range of normal stress levels.

An issue of primary importance is the determination of whether, during slip across faults at shallow depths, the interface dilates or contracts, with direct implications to the critical pore pressure required for slip in induced seismicity studies, and sliding instabilities in general. We find that during unloading in stick slip cycles, the sample typically contracts, a process that could prompt excess pore pressure in the fault aperture, which might consequently trigger an induced seismicity event,

given the necessary conditions in the field. On the other hand, we find that during stick phases the interfaces typically dilate, a process that can apparently increase the strength of the sheared interface due to increasing frictional resistance as well as decreased pore pressure in the fault aperture. We note that pore pressures were not directly studied here experimentally, but the relationship between vertical motions and pore pressure during shear, at least in undrained conditions, is rather straightforward. Another important implication of our study to fault mechanics is the energy budget during shear across the fault during stick-slip type of motion. We propose below a procedure to assess the potential for unstable motion across the fault in terms of energy stored and released during stick and slip segments, respectively.

#### 6.4. Stored elastic strain energy during stick phases

We have observed that the highest magnitude of stress drops is associated with a specific roughness level, here coinciding with saw-cut roughness. We propose that the reason for this criticality is that during 'stick' segments the greatest amount of elastic strain energy is accumulated and stored in the loading system before its spontaneous release during the 'slip' segment. We suggest that the stored elastic strain energy in the system is scalable to the amount of dissipated energy as a laboratory earthquake at the consequent slip phase, which in essence is controlled by the stress drop and amount of displacement during the slip segment. It is important to note that this energy component does not represent the stored elastic energy within the fault but rather recording the available energy in the shear loading system ("the spring") for the next spontaneous event.

Fig. 11 illustrates the scheme for measuring the elastic strain energy stored in the spring during a stick phase. During this stage, the sample remains in quasi-static conditions, ensuring equilibrium. Consequently, the force measurement by the shear load cell represents the global shear resistance of the interface. Therefore, the stored elastic strain energy can be measured by integrating the area between the piston and interface (labeled shear box in the figure) force curves across the corresponding shear displacement, measured by the piston transducer and the two horizontal LVDTs that are mounted directly on the shear box, respectively.

The triangle (ABC) delineated in Fig. 11 represents the accumulated elastic strain energy between the spring and the interface which is responsible for initiating unstable sliding. We examine each stick phase

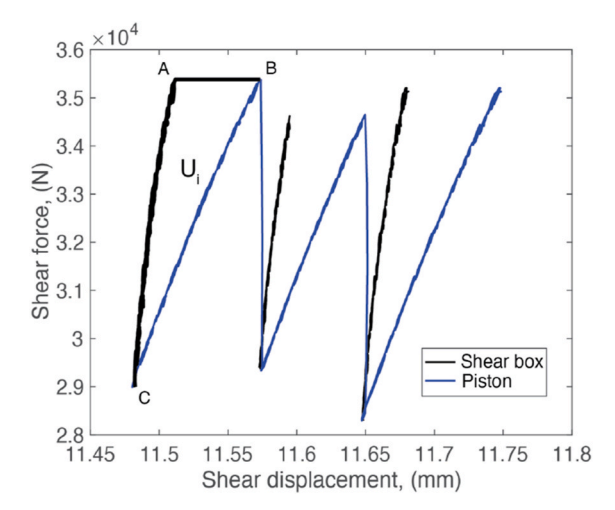


**Fig. 11.** Typical behavior of stick-slip sliding on a saw-cut interface including the shear piston (black) and Shear box (blue) displacements. The area delineated by triangle ABC represents the elastic stored energy in the shear load frame (the spring) during a stick phase. (For interpretation of the references to color in this figure legend, the reader is referred to the Web version of this article.)

individually and measure the stored elastic strain energy during a stick segment, represented mathematically as follows:

$$U_i = \int_{u_o}^{u_f} F du; \quad u = u_{piston} - u_{box}$$
 (7)

where  $U_i$  is the accumulated strain energy at the spring during the stick phase,  $u_o$  and  $u_f$  are the differences between the piston ( $u_{piston}$ ) and shearbox ( $u_{box}$ ) displacement at the beginning and end of a stick cycle, and F is the shear load applied by the system.

Therefore, subtracting the integrated displacement output of the piston by the shear box provides the stored elastic energy in the shear load frame. The shear-box displacement  $u_{box}$  for a given force range F which is equivalent to the intracyclic shear stiffness (note the shear stiffness is strictly defined as shear stress divided by shear displacement) varies between tests as it is strongly dependent upon the initial surface roughness and the level of normal stress (see Fig. 8). This means that in general, for any amount of shear force buildup during an arbitrary stick phase, interfaces with higher shear stiffness (black lines in Fig. 11) would yield a greater difference in displacement between the piston and the shear-box, resulting in a greater amount of contraction in the system's spring analogue. Recalling that the machine stiffness is generally constant (Fig. 8, upper panels) and invoking Hoeke's law, the greater the contraction experienced by the loading system, the greater the potential elastic energy accumulated in the system during stick segments available for spontaneous release during the subsequent slip phase, which is scaled by the magnitude of the corresponding stress drop. We suggest, therefore, that interfaces with greater shear stiffness will accumulate more elastic strain energy in the spring during shear force buildup in stick phases and consequently will generate stronger laboratory earthquakes. We further show in Fig. 12 that the calculated elastic strain energy in stick segments is indeed roughness and normal stress dependent, with the Sawcut interfaces exceeding both the smoothed and fractured surfaces.

The accumulated elastic strain energy during stick phases as a function of initial roughness and normal stress is presented graphically in Fig. 13 as a surface plot. It can be seen that sawcut interfaces, which consistently record the highest stress drop and shear stiffness values, also show the largest amount of stored elastic strain energy at the end of stick phases, for any given normal stress tested in this study. As in the 'critical roughness' concept, which was defined for stress drops, <sup>57</sup> the total stored elastic strain energy at the end of stick cycles decreases to both ends of the studied roughness spectrum.

## 7. Summary and conclusion

We performed direct shear tests with different fault roughness and under different normal stress levels to study and characterize the nature of stick slip motion both parallel and vertical to shear direction. Key parameters such as the intracyclic shear stiffness, stress drop magnitude, and vertical motion (dilation) were measured and analyzed as a function of initial surface roughness, normal stress level, and amount of shear displacement.

By detrending the vertical motion output during the steady state regime of the test (i.e., 8–10 mm of shear displacement), we found that the vertical motion within stick slip cycles is highly sensitive to initial roughness levels and normal stress. We found that in most cases, the vertical motion during the loading stage of the stick slip cycle is dilational, where the only exceptions are rough faults that were sheared under low normal stress. The "in phase" interactions between dilation and stress drops as typically observed in sawcut faults are attributed to different asperity interaction mechanisms.

For the intracyclic stress drop and shear stiffness measurements we found that the '*critical roughness*' concept presented by Morad et al. <sup>57</sup> remains valid for a wider range of normal stresses, from 2.5 to 15 MPa

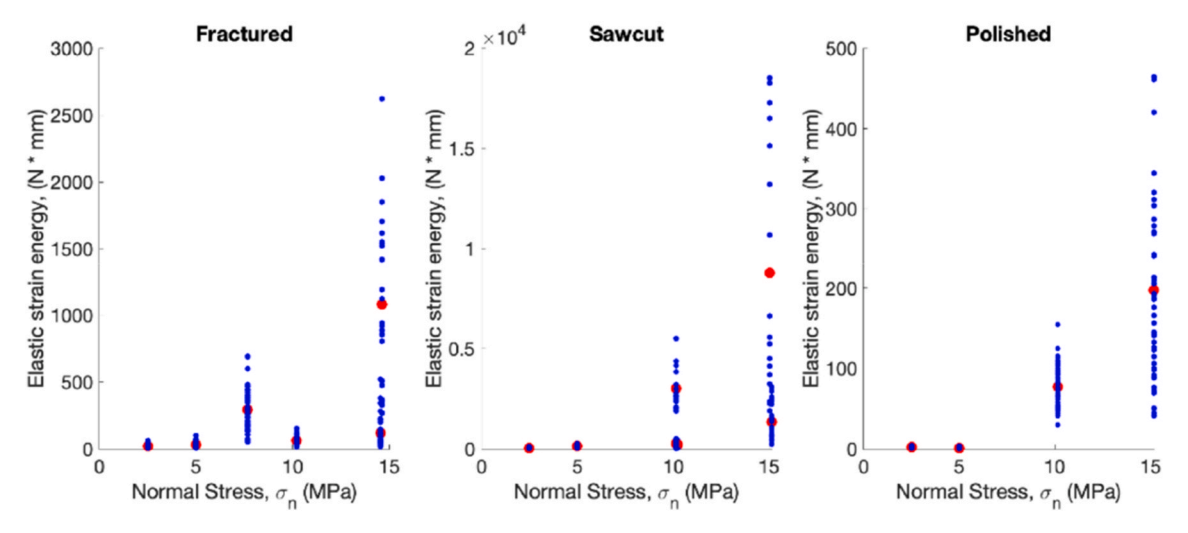
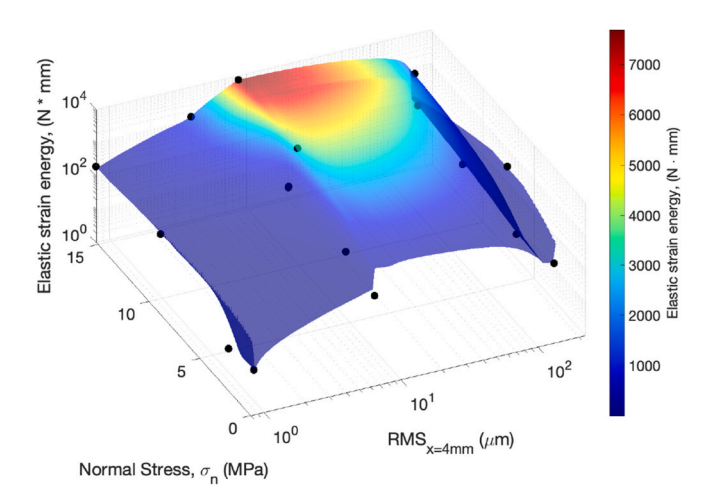


Fig. 12. Elastic stored energy as inferred from Eq. (7) for the three levels of roughness and normal stress. The red points represent the average stored energy per experiment. The data was taken during residual friction usually between 4 and 10 mm displacement. (For interpretation of the references to color in this figure legend, the reader is referred to the Web version of this article.)



**Fig. 13.** The stored elastic strain energy in the shear load frame during stick phases as a function of surface roughness and normal stress. Note X and Z axes are in logarithmic scale.

for the same type of Diabase laboratory faults. We confirm here that the 'critical roughness' that generated the strongest stress drops corresponds also in this study to the saw-cut interfaces, with mean roughness of 10  $\mu m$ , as also reported by Morad et al., 2022. The shear stiffness, measured along the linear segment of reloading phases of stick slip cycles, was also found to be highest for the saw-cut surfaces.

We propose here, based on an energetic approach, that the elastic stored energy between the piston (representing remote field stresses) and the shear block (representing the fault) can be used to predict the magnitude of sliding instability comparing to the well-established relationship between the critical and machine stiffnesses  $(k_c \cdot k_m)$  because  $k_i$  can be measured in every stick – slip cycle whereas  $k_c$  can only be calculated, based on empirically obtained rate and state parameters. Moreover, when sliding is very unstable with a lot of noise generated by frequent stick-slip oscillations, ideal "steady state" sliding, which is necessary for retrieving rate and state parameters, is never reached, rendering calculation of  $k_c$  impossible.

We propose that the observed variation in the dynamic behavior of rough fractured interfaces with shear displacement under high normal stresses suggests that shearing-through asperities mechanism can be divided into two main stages: 1) an early stage where most damage is brittle, during which relatively large intact wear particles are detached and accumulated along the interface, and 2) a later stage where these large particles disintegrate and comminute as sliding progresses, affecting the overall sliding behavior in the process.

#### CRediT authorship contribution statement

Eliaz Ishay: Writing – original draft, Visualization, Validation, Methodology, Investigation, Formal analysis, Data curation. **Doron Morad:** Writing – review & editing, Validation, Investigation, Formal analysis, Data curation. **Yossef H. Hatzor:** Writing – review & editing, Supervision, Resources, Project administration, Methodology, Investigation, Funding acquisition, Conceptualization.

## **Funding sources**

This work is supported by Israel Science Foundation through grant number 2234/21 awarded to Y. H. Hatzor. E. Ishay thanks Israel Ministry of Energy and Infrastructure for a student fellowship No. 352899.

# Declaration of competing interest

The authors declare the following financial interests/personal relationships which may be considered as potential competing interests: Yossef H. Hatzor reports financial support was provided by Israel Science Foundation. Y.H.H. serves on the editorial board of IJRMMS. If there are other authors, they declare that they have no known competing financial interests or personal relationships that could have appeared to influence the work reported in this paper.

## Acknowledgements

We thank Yuval Tal and Amir Sagy for assistance with laboratory fault roughness measurements. Yuval Tal is also thanked for critically reviewing an early draft of this paper. We dedicate this paper to the memory of the late Professor R. E. Goodman of UC Berkeley, whose work on friction and dilation through shear across rock discontinuities has greatly inspired this research.

## Data availability

Data generated and used in this research can be downloaded at: Ishay, E., Morad, D., & Hatzor, Y. H. (2025). Dataset for: Micro-

mechanics of stick-slip deformation across rough faults [Data set]. Zenodo. https://doi.org/10.5281/zenodo.15687794.64

#### References

- 1. Bowden FP, Tabor D, Palmer F. The friction and lubrication of solids. Am J Phys. 1951;19(7):428-429. https://doi.org/10.1119/1.193301
- 2. Dieterich JH, Kilgore BD. Direct observation of frictional contacts: new insights for state-dependent properties. PAGE. 1994;143(1):283-302. https://doi.org/10.1007/
- Rubinstein SM, Cohen G, Fineberg J. Detachment fronts and the onset of dynamic friction. Nature. 2004;430(7003):1005-1009. https://doi.org/10.1038/
- Archard JF, Allibone TE. Elastic deformation and the laws of friction. Proceedings of the Royal Society of London Series A Mathematical and Physical Sciences. 1997;243(1233):190–205. https://doi.org/10.1098/rspa.1957.0214.
- 5. Mei C, Wu W. Fracture asperity evolution during the transition from stick slip to stable sliding. Philos Trans R Soc A Math Phys Eng Sci. 2021;379(2196), 20200133. https://doi.org/10.1098/rsta.2020.0133
- 6. Persson BNJ, Albohr O, Tartaglino U, Volokitin AI, Tosatti E. On the nature of surface roughness with application to contact mechanics, sealing, rubber friction and adhesion. J Phys Condens Matter. 2004;17(1), R1. https://doi.org/10.1088/
- 7. Morad D, Lyakhovsky V, Hatzor YH, Sagy A. Stress heterogeneity and the onset of faulting along geometrically irregular faults. Geophys Res Lett. 2022;49(17), e2021GL097591. https://doi.org/10.1029/2021GL097591.
- Tal Y, Hager BH, Ampuero JP. The effects of fault roughness on the earthquake nucleation process. J Geophys Res Solid Earth. 2018;123(1):437-456. https:/ org/10.1002/2017.JB0147
- 9. Goebel THW, Kwiatek G, Becker TW, Brodsky EE, Dresen G. What allows seismic events to grow big?: insights from b-value and fault roughness analysis in laboratory stick-slip experiments. Geology. 2017;45(9):815–818. https://doi.org/10.1130/
- 10. Ohnaka M. A constitutive scaling law and a unified comprehension for frictional slip failure, shear fracture of intact rock, and earthquake rupture. J Geophys Res. 2003; 108(B2), 2000JB000123. https://doi.org/10.1029/2000JB000123.
- 11. Tal Y, Goebel T, Avouac JP. Experimental and modeling study of the effect of fault roughness on dynamic frictional sliding, Earth Planet Sci Lett. 2020;536, 116133. https://doi.org/10.1016/j.epsl.2020.116133.
- 12. Tal Y, Faulkner D. The effect of fault roughness and earthquake ruptures on the evolution and scaling of fault damage zones. J Geophys Res Solid Earth. 2022;127(1), e2021JB023352, https://doi.org/10.1029/2021JB023352
- 13. Lee J, Tsai VC, Hirth G, Chatterjee A, Trugman DT. Fault-network geometry influences earthquake frictional behaviour. Nature. 2024;631(8019):106-110. https://doi.org/10.1038/s41586-024-07518-6
- 14. Siman-Tov S, Aharonov E, Sagy A, Emmanuel S. Nanograins form carbonate fault mirrors. Geology. 2013;41(6):703-706. https://doi.org/10.1130/G34087
- Sagy A, Brodsky EE, Axen GJ. Evolution of fault-surface roughness with slip.
- *Geology.* 2007;35(3):283–286. https://doi.org/10.1130/G23235A.1.

  16. Brace WF, Paulding BW, Scholz C. Dilatancy in the fracture of crystalline rocks. J Geophys Res. 1966;71(16):3939-3953. https://doi.org/10.1029/ JZ071i016p03939.
- 17. Zhou H, Grasselli G. Dilation of rock joints based on quantified surface description: Ultimate dilation, ARMA-2018-1169, 2018.
- 18. Fang Y, Elsworth D, Wang C, Ishibashi T, Fitts JP. Frictional stability-permeability relationships for fractures in shales. J Geophys Res Solid Earth. 2017;122(3): 1760-1776. https://doi.org/10.1002/2016JB013435.
- 19. Zhou H, Abdelaziz A, Grasselli G. In: Rock Dilation and Its Effect on Fracture Transmissivity. 2018, D033S052R003. https://doi.org/10.15530/URTEC-2018-
- Ellsworth WL. Injection-Induced earthquakes. Sci. 2013;341(6142), 1225942. https://doi.org/10.1126/science.1225942.
- 21. Grigoli F, Cesca S, Priolo E, et al. Current challenges in monitoring, discrimination, and management of induced seismicity related to underground industrial activities: a European perspective. Rev Geophys. 2017;55(2):310-340. https://doi.org/
- 22. Aben FM, Brantut N. Dilatancy stabilises shear failure in rock. Earth Planet Sci Lett. 2021;574, 117174. https://doi.org/10.1016/j.epsl.2021.11717
- 23. Brantut N. Dilatancy-induced fluid pressure drop during dynamic rupture: direct experimental evidence and consequences for earthquake dynamics. Earth Planet Sci Lett. 2020;538, 116179. https://doi.org/10.1016/j.epsl.2020.116179
- 24. Hamiel Y, Lyakhovsky V, Agnon A. Poroelastic damage rheology: dilation, compaction, and failure of rocks. G-cubed. 2005;6(1). https://doi.org/10.1029/
- 25. Marinho FAM, do Amaral Vargas Jr E. Effect of suction on the shear strength of soil-rock interfaces. Geotech Geol Eng. 2020;38(6):6145-6155. https://doi. 10.1007/s10706-020-01421-3.
- Jaeger JC, Cook NGW, Zimmerman RW. Fundamentals of Rock Mechanics. fourth ed. Blackwell Pub; 2007.
- Rabinowicz E. Stick and slip. Sci Am. 1956;194(5):109-119.
- 28. Finnegan NJ, Brodsky EE, Savage HM, Nereson AL, Murphy CR. Seasonal slow landslide displacement is accommodated by mm-Scale stick-slip events. Geophys Res Lett. 2022;49(20), e2022GL099548. https://doi.org/10.1029/2022GL099548

- 29. Yamada M, Mori J, Matsushi Y. Possible stick-slip behavior before the Rausu landslide inferred from repeating seismic events. Geophys Res Lett. 2016;43(17): 9038-9044. https://doi.org/10.1002/2016GL069288
- Fischer UH, Clarke GKC. Stick-slip sliding behaviour at the base of a glacier. Ann Glaciol. 1997;24:390-396. https://doi.org/10.3189/S0260305500012490
- 31. Helmstetter A. Repeating low frequency icequakes in the mont-blanc massif triggered by snowfalls. J Geophys Res: Earth Surf. 2022;127(12), e2022JF006837. https://doi.org/10.1029/2022JF006837.
- 32. Lacroix P, Belart JMC, Berthier E, Sæmundsson b, Jónsdóttir K. Mechanisms of landslide destabilization induced by glacier-retreat on tungnakvíslarjökull area, Iceland. Geophys Res Lett. 2022;49(14), e2022GL098302. https://doi.org/10.1029/
- 33. Bartali R, Sarocchi D, Nahmad-Molinari Y. Stick-slip motion and high speed ejecta in granular avalanches detected through a multi-sensors flume. Eng Geol. 2015;195: 248-257. https://doi.org/10.1016/j.enggeo.2015.06.019
- Cueto-Felgueroso L, Santillán D, Mosquera JC. Stick-slip dynamics of flow-induced seismicity on rate and state faults. Geophys Res Lett. 2017;44(9):4098-4106. https:// doi.org/10.1002/2016GL072045.
- Yao Z, Fang Y, Zhang R, et al. The mechanism of stick-slip as a rockburst source in jointed rockmass: an experimental Study. Rock Mech Rock Eng. 2023;56(5): 3573-3593. https://doi.org/10.1007/s00603-023-03220-
- 36. Ji Y, Wu W, Zhao Z. Unloading-induced rock fracture activation and maximum seismic moment prediction. Eng Geol. 2019;262, 105352. https://doi.org/10.1016/j.
- 37. Meng F, Zhou H, Wang Z, et al. Experimental study on the prediction of rockburst hazards induced by dynamic structural plane shearing in deeply buried hard rock tunnels. Int J Rock Mech Min Sci. 2016;86:210-223. https://doi.org/10.1016/j
- 38. Anthony JL, Marone C. Influence of particle characteristics on granular friction. J Geophys Res Solid Earth. 2005;110(B8). https://doi.org/10.1029/2004JB003399.
- Brace WF. Laboratory studies of stick-slip and their application to earthquakes. Tectonophysics. 1972;14(3-4):189-200. https://doi.org/10.1016/0040-1951(72)
- 40. Rabinowicz E. The intrinsic variables affecting the stick-slip process. Proc Phys Soc. 1958;71(4):668–675. https://doi.org/10.1088/0370-1328/71
- 41. Stesky RM. Rock friction-effect of confining pressure, temperature, and pore pressure. PAGE. 1978;116(4-5):690-704. https://doi.org/10.1007/BF00876532
- 42. Dieterich JH. Time-dependent friction and the mechanics of stick-slip. PAGE. 1978; 116(4):790-806. https://doi.org/10.1007/BF00876539.
- Leeman JR, Saffer DM, Scuderi MM, Marone C. Laboratory observations of slow earthquakes and the spectrum of tectonic fault slip modes. Nat Commun. 2016;7(1), 11104, https://doi.org/10.1038/ncomms11104.
- Marone C. LABORATORY-DERIVED FRICTION LAWS AND THEIR APPLICATION TO SEISMIC FAULTING. Annu Rev Earth Planet Sci. 1998;26:643-696. https://doi.org/ 10.1146/annurev.earth.26.1.643, 1998:26,
- 45. Ruina A. Slip instability and state variable friction laws. J Geophys Res Solid Earth.
- 1983;88(B12):10359-10370. https://doi.org/10.1029/JB088iB12p10359. Scholz CH. *The Mechanics of Earthquakes and Faulting*. Cambridge University Press;
- 47. Tinti E, Scuderi MM, Scognamiglio L, Di Stefano G, Marone C, Collettini C. On the evolution of elastic properties during laboratory stick-slip experiments spanning the transition from slow slip to dynamic rupture. J Geophys Res Solid Earth. 2016;121 (12):8569–8594. https://doi.org/10.1002/2016JB013545.

  48. Lockner DA, Kilgore BD, Beeler NM, Moore DE. The transition from frictional sliding
- to shear melting in laboratory stick-slip experiments. In: Fault Zone Dynamic Processes. American Geophysical Union (AGU); 2017:103-131. https://doi.org/ 10.1002/9781119156895
- 49. Byerlee JD, Brace WF. Stick slip, stable sliding, and earthquakes—Effect of rock type, pressure, strain rate, and stiffness. J Geophyl Res (1896-1977). 1968;73(18): 6031-6037. https://doi.org/10.1029/JB073i018p06031
- Gu JC, Rice JR, Ruina AL, Tse ST. Slip motion and stability of a single degree of freedom elastic system with rate and state dependent friction. J Mech Phys Solid. 1984;32(3):167–196. https://doi.org/10.1016/0022-5096(84)90007-
- 51. Hudson JA, Crouch SL, Fairhurst C. Soft, stiff and servo-controlled testing machines: a review with reference to rock failure. Eng Geol. 1972;6(3):155-189. https://doi. rg/10.1016/0013-7952(72)90001-4
- 52. Dieterich JH. Modeling of rock friction: 1. Experimental results and constitutive equations. J Geophys Res. 1979;84(B5):2161-2168. https://doi.org/10.102 JB084iB05p02161.
- 53. Okubo PG, Dieterich JH. Effects of physical fault properties on frictional instabilities produced on simulated faults. J Geophys Res Solid Earth. 1984;89(B7):5817-5827. https://doi.org/10.1029/JB089iB07p05817
- 54. Brown SR, Scholz CH. Broad bandwidth study of the topography of natural rock surfaces. J Geophys Res Solid Earth. 1985;90(B14):12575-12582. https://doi.org/ 10.1029/JB090iB14p12575.
- Candela T, Renard F, Klinger Y, Mair K, Schmittbuhl J, Brodsky EE. Roughness of fault surfaces over nine decades of length scales. J Geophys Res Solid Earth. 2012;117 (B8). https://doi.org/10.1029/2011JB009041
- Power WL, Tullis TE, Brown SR, Boitnott GN, Scholz CH. Roughness of natural fault surfaces. Geophys Res Lett. 1987;14(1):29-32. https://doi.org/
- 57. Morad D, Sagy A, Tal Y, Hatzor YH. Fault roughness controls sliding instability. Earth Planet Sci Lett. 2022;579, 117365. https://doi.org/10.1016/j.

- Brodsky EE, Kirkpatrick JD, Candela T. Constraints from fault roughness on the scale-dependent strength of rocks. *Geology*. 2016;44(1):19–22. https://doi.org/ 10.1130/037706.1
- Power WL, Tullis TE, Weeks JD. Roughness and wear during brittle faulting. J Geophys Res. 1988;93(B12):15268–15278. https://doi.org/10.1029/ JB093iB12p15268.
- Muralha J, Grasselli G, Tatone B, Blümel M, Chryssanthakis P, Yujing J. ISRM suggested method for laboratory determination of the shear strength of rock joints: revised version. *Rock Mech Rock Eng.* 2014;47(1):291–302. https://doi.org/10.1007/s00603-013-0519-z.
- Morad D, Sagy A, Hatzor YH. The significance of displacement control mode in direct shear tests of rock joints. *Int J Rock Mech Min Sci.* 2020;134, 104444. https://doi.org/10.1016/j.ijrmms.2020.104444.
- Meng F, Wang F, Wong LNY, et al. Shear behavior and off-fault damage of saw-cut smooth and tension-induced rough joints in granite. *J Rock Mech Geotech Eng.* 2024; 16(4):1216–1230. https://doi.org/10.1016/j.jrmge.2023.07.008.
- Chen X, Carpenter BM, Reches Z. Asperity Failure Control of Stick–Slip Along Brittle Faults. Pure Appl Geophys. 2020;177(7):3225–3242. https://doi.org/10.1007/ s00024-020-02434-v.
- [Data set] Ishay E, Morad D, Hatzor YH. Dataset for: Micromechanics of stick-slip deformation across rough faults. Zenodo. 2025. https://doi.org/10.5281/ zenodo.15687794.